DOI: 10.1002/ ((please add manuscript number))
Article type: Full paper

Hierarchical domain structure and extremely large wall current in epitaxial $BiFeO_3$ thin films

Zi Long Bai, Xiao Xing Cheng, Dong Fang Chen, David Wei Zhang, Long-Qing Chen, James F. Scott, Cheol Seong Hwang, An Quan Jiang**

Dr. Zi Long Bai, Dr. Dong Fang Chen, Prof. David Wei Zhang and Prof. An Quan Jiang

State Key Laboratory of ASIC & System, School of Microelectronics, Fudan University, Shanghai 200433, China.

E-mail: aqjiang@fudan.edu.cn.

Dr. Xiao Xing Cheng and Prof. Long-Qing Chen

Department of Materials Science and Engineering, The Pennsylvania State University, University Park, Pennsylvania 16802, USA.

Prof. James F. Scott

Departments of Chemistry and Physics, St. Andrews University, St. Andrews, KY16 9ST, UK.

Prof. Cheol Seong Hwang

Department of Materials Science and Engineering and Inter-University Semiconductor Research Center, Seoul National University, Seoul 151-744, Korea.

E-mail: cheolsh@snu.ac.kr

Keywords: hierarchical domains; domain wall; multiple rotations; wall current; ferroelectric domain-wall memory

Abstract Erasable electrical conductive domain walls in an insulating ferroelectric matrix provide novel functionalities for applications in logic and memory devices. The crux of such success requires sufficiently high wall currents to drive high-speed and high-power nanodevices. This work provides an appealing strategy to increase the current by two orders of magnitude through the careful selection of current flowing paths along the charged walls. The dense walls come into form through the hierarchical evolution of the 71°, 109° and 180° domains of epitaxial $BiFeO_3$ films in a planar-geometry ferroelectric resistance-switching memory cell. The engineered films grown on $SrTiO_3$ and $GdScO_3$ substrates allow the observation of detailed local configurations and the evolution of the different domain types using vector[Revs 2 and 3] piezo-force microscopy. The higher local electrical conductivity near the charged domain walls was identified by conductive atomic-force microscopy. It is shown that 180° domain reversal proceeds by three-step 71° rotations of the pristine domains. Surprisingly, a maximum current of ~300 nA was observed for current paths[Rev1-1] along charge-uncompensated head-to-head hierarchical domain walls connecting the two electrodes on the film surface. Furthermore, the achievable current level can be conveniently controlled by varying the relative directions of the initial polarization and the applied field.

1. Introduction

Ferroelectric materials have switchable bound charges associated with their spontaneous polarization that are the main assets for the use of these materials in a diverse range of functional electronic devices, including ferroelectric memory devices.[1] As in other charge-based memory devices, the limited polarization charge per unit area of most well-known ferroelectric materials imposes a significant scaling challenge for charge-based electronic devices such as the one-transistor/one-capacitor ferroelectric random access memory (1T-1C FRAM). As an alternative, resistance-based ferroelectric memory devices such as ferroelectric tunnel junction-based memories[2-4] have attracted a great deal of attention, but the polarization direction-dependent tunneling mechanism imposes fundamental limitations on device scaling and reliability. The possible involvement of a defect-mediated resistance switching mechanism, which is mostly related to oxygen vacancies, also complicates the precise operation of a device.[5]

Recently the authors reported a completely different resistance-based ferroelectric device based on the temporal creation and elimination of conductive domain walls in epitaxial $BiFeO_3$ (BFO) thin film.[6] Unlike other conventional ferroelectric devices, this device has a lateral memory cell geometry that allowed the examination of several highly intriguing properties of this unique ferroelectric material. The ferroelectric domain walls can be created, moved, and repositioned via partial domain switching under an electric field applied in the opposite direction to the polarization direction of the unswitched bulk matrix.[6-16] While the work produced a truly ground-breaking new device concept that alleviated almost all the scaling- and reliability-related issues for ultra-high-density ferroelectric memory applications, two main issues arose. First, the mechanism involved in the switching of the ferroelastic (71° and 109°) and ferroelectric (180°) domains is not yet understood. Second, the attainable wall current (which was previously a maximum of 14 nA) must be further improved, and the upper limit of the maximum attainable

current must be determined. It should be reminded that for most commercial memory devices for which application is envisioned, a mimimum wall current should be ~0.1 μA to obtain read times of 10 ns.[17,18]

Understanding the domain switching mechanism has implications for achieving the maximum attainable wall current that requires the knowledge of the domain evolution process in different geometrical configurations under an applied voltage, along with their correlation with the local and global electrical conductivities. The state-of-the-art vector piezo-force microscopy (V-PFM) and conductive atomic-force microscopy (CAFM) techniques are highly useful in this regard, particularly in conjunction with nanofabrication techniques for devices with different electrode geometries because they allow arbitrary control of the applied field direction with respect to the crystallographic and domain directions of the BFO films and make detailed studies of the domain evolution process possible. It is surprisingly found in this work that 180° domain switching can process through three-step 71° rotations in some cases rather than the general prediction of two-step 71° and 109° rotations only.[19] In other words, 109° domain switching is two-step 71° rotations that are not easily discerned in several other experiments. Rev 1-2

However, most of the temporarily formed domains and their walls dissipate rapidly over time, which prohibits the above investigations. Therefore, in this work, three different types of epitaxial BFO thin films on $SrTiO_3$ (STO) and $GdScO_3$ (GSO) substrates were prepared through extensive optimization of the pulsed laser deposition (PLD) technique. These structures are 120-nm-thick BFO (001)/GSO (110), 120-nm-thick BFO (110)/STO (110), and 35-nm-thick BFO (001)/STO (001) films, where (001) and (110) represent the crystallographic planes in terms of cubic crystal symmetry (pseudocubic symmetry for BFO) (see Methods). The films with different thicknesses show the evolution of the hierarchical domains with geometrically limited wall currents; once the near-surface switched domains are thickened enough to touch the substrates

(i.e., the wall currents in 120-nm-thick BFO at high fields are much higher than those in 35-nm-thick BFO). [Rev1-3] The BFO (001)/GSO (110) sample showed a surprisingly long retention time (~3 h) for the voltage-induced domains and walls, which allowed these domains and walls to be examined carefully by V-PFM and CAFM. The pristine BFO film showed a striped domain pattern with average periodicity of ~200 nm in which domains change relative to the applied lateral field strength. This was critically important to the study because it revealed that the domain switching process proceeds via hierarchical formation of the coexisting 71° domains, the 109° domains, and eventually the 180° domains, with increasing voltage. The second sample, i.e., the BFO (110)/STO (110) structure, showed a completely homogeneous domain pattern in the pristine state, which provided a feasible and unique platform for control of the domain patterns and the wall currents along the different crystallographic directions of the BFO layer. In conjunction with the first sample, it was unambiguously determined that the head-to-head 180° domain wall, which was eventually formed by process of hierarchical domain propagation through the 71° and 109° rotations, can provide an exceptionally high current of ~300 nA. This value exceeds the highest previously reported value (14 nA) by more than an order of magnitude. [6]. This is also a practical demonstration of the long-term conjecture that the charge-uncompensated domain boundaries form the current flow paths in insulating ferroelectric materials.[20,21] (Rev 1-3) The final sample, i.e., the BFO (001)/STO (001) structure, is used to show the evolution of the hierarchical domains under different coercive fields.

This work also contributes to the critical understanding of the properties of domain walls with different orientations, which has previously been impossible in the out-of-plane direction of metal/ferroelectric/metal-type capacitors. In addition, the involvement of only one type of domain wall or difficulty in aligning the charge-uncompensated domain walls along the read-field direction has hampered observation of the high wall current. This work, therefore, provides a step

forward in terms of both practical application and fundamental understanding of ferroelectric domain wall-related phenomena.

2. Results and Discussion

2.1. Temporal creation of hierarchical domain structure

The topographic atomic force microscopy (AFM) images in Supplementary Figure S1a show terraces composed of atomic steps with root-mean-square roughness values of 0.64 nm for the BFO (001)/GSO (110) structure and 0.17 nm for the BFO (001)/STO (001) structure. Reciprocal space mapping and X-ray diffraction (XRD) studies (Supplementary Figure S1b) confirmed (001) BFO orientations on both the (001) STO and (110) GSO substrates but (110) BFO orientations were found on the (110) STO substrates.[9] A careful V-PFM study showed that all the films have out-of-plane polarizations pointing towards the bottom substrates, whereas the in-plane polarization state is different for each of the thin films. After film deposition, a Pt thin film was deposited and patterned to form two Pt top electrodes, designated TE1 and TE2, with various widths (*w*) and gap lengths (*l*) by a combination of electron beam lithography and ion milling (see Methods). During electrical testing, a voltage was applied to TE1 while TE2 was grounded. When a sufficiently high read voltage was applied in short time (~ns), [Rev 1-4] the transient creation of conductive charged walls via a partial domain reversal was observed near the film surface between TE1 and TE2 and was accompanied by the flow of an "on" current.[6] However, these domain walls disappeared from the BFO (001)/STO (001) sample immediately after the removal of the read voltage because of the high depolarization and ferroelastic energies. However, the periodic stripe domains of the BFO (001) films on the (110) GSO substrates can reduce these energies and thus greatly increase the domain back-switching time, which made it possible to examine these domain configurations using V-PFM after a long time (~s) poling voltage.[22,23]

The significant charge injection occurs under a long time poling voltage that can temporally compensate the depolarization field delaying the domain back-switching.[6] For the information writing in real memories, the films should be etched into a mesa structure with two side electrodes deposited. This forms a parallel-plate like capacitor, where the domain under a short-time (~ns) write voltage higher than a coercive voltage applied to the two side electrodes has good retention.[6] Rev1-4

Figure 1a (left panel) shows the areal distribution of the initial variants of the r1− to r4− domains (indicated by the coloured arrows in the inset of the right panel). The pristine film consists of stripe 71° walls by r2- and r3- variants only within the nanogap of a BFO (001)/GSO (110) device with w/l= 1000 nm/500 nm. After switching at +/- 20 V for a dozen of cycles, the newly formed r1- and r4- domains repeatedly appeared after poling of the device at +15 V, but disappeared after a long relaxation time (Supplementary Figure S2).Rev3-5 The double current-voltage (I-V) sweep shown in the right panel shows repeatable two-step jumps in the "on" current at V_{c1} and V_{c2}. After the sample was switched using a bias voltage of −15 V, which is higher than V_{c2} but lower than V_{c1}, for a period of 10 s, a switched domain image was captured and showed a triangular domain shape. Two of the domain's sides were composed of a large proportion of the 71° walls and a small proportion of the 109° walls that connect TE1 and TE2, as shown in Figure 1b. The right panel shows the areal distribution of the rotation angles for all variants, which was produced by comparing the V-PFM images after poling at +15 V and switching at −15 V. It should be noted that most of these domains experienced the 71° rotation within the triangular region, except for two small corners that experienced 109° rotations. Therefore, the first jump in the "on" current at V_{c1} in the I-V curve shown in Figure 1a (right panel) is correlated with the 71° rotation of all the domain variants that form the two bridging walls shown in Figure 1b. These newly formed walls are more electrically conductive than the pristine stripe walls, in which the

uncompensated ferroelectric bound charges were largely compensated by charged mobile defects during film deposition at high temperatures (Supplementary Figure S3a and b).[24] The device was then switched back to the initial poled state by applying the poling voltage of +15 V again, as inspected by V-PFM imaging, Rev3-5 and was subsequently switched to a new "on" state by application of a switching voltage of −17 V (< V_{c2}). Both the r4− and r1− domains grew to form the three penetrating 71° and 109° walls that connected TE1 and TE2, as shown in Figure 1c (left panel). Use of this new wall configuration led to a significant increase in the "on" current. The areal distribution of the rotation angles shown in the right panel of Figure 1c indicates that several of the previous 71° domains experienced further 71° rotations during growth of the 109° domain at V_{c2}, which implies that a hierarchical domain pattern may be involved (note that two sequential 71° rotations results in a 109° domain rather than a 142° domain; see the inset in the right panel of Figure 1a). A full exploration of the grown hierarchical domain pattern requires the acquisition of the domain information after the 180° switching process at voltages higher than a coercive voltage of V_{c3}. However, the retention times of the switched domains at voltages >V_{c3} were too short for V-PFM domain images to be recorded when imaging was attempted using devices with l = 500 nm. This problem was resolved by adopting a device with l = 1000 nm, in which the domain grew throughout the entire film thickness and thus reduced the depolarization field.[13] Therefore, after switching at −20 V for 30 s, the growth of two triangular r1− and r3+ domains was observed based on the 71°, 109° and 180° rotations of the pristine r2− and r3− variants in 71° steps with three jumps of "on" currents in their *I-V* curves (Supplementary Figure S4a and b). Rev1-6 These results showed that 180° domain reversal at voltages >V_{c3} could be achieved using hierarchical multiple (1-3 step) 71° rotations of all the variants of the pristine domains.

Each penetrating domain growth that connected TE1 and TE2 also increased the conductive wall number and thus the "on" current, which was observed as multiple jumps in the "on" currents in the *I*-*V* curves. Supplementary Figure S5a–e summarize the three types of "on" current jumps that occurred at the specific coercive voltages of V_{c1}, V_{c2}, and V_{c3}, which imply sequential formation of the 71°, 109° and 180° domains, respectively, with increasing field strength. The current jump at V_{c3} predicts the onset of the 180° domain rotation, which was corroborated by the results in the V-PFM images in Supplementary Figure S4a and b. [Rev1-7]

2.2. CAFM current mapping of charged and neutral walls

Domain walls can be either neutral or charged, depending on the relative orientations of the polarization directions of the two adjacent domains and the degree of compensating carrier trapping that occurs at the domain walls. It was previously reported that the conductivity of charged walls has the highest value,[7-14] but precise identification of the correlation between domain wall type and conductivity has lacked, despite its importance for device applications. In this work, this task has been accomplished using two methods: CAFM mapping of the retained domain walls in the BFO (001)/GSO (110) sample, and variation of the surface electric field direction relative to the uniform polarization of the BFO (110)/STO (110) sample.

Figure 2a shows a CAFM current mapping image of a BFO (001)/GSO (110) nanodevice with w/l = 1000 nm/1000 nm after switching at −25 V. Application of the −25 V switching voltage induced the formation of triangular domains (as per the case in Figure 1b), but these domains collapsed into several segments after a retention time of ~30 min. Under these circumstances, the CAFM and V-PFM images could be acquired from the same area, which allowed the authors to identify the correlation between the domain wall type and the local electrical conductivity precisely. In Figure 2a, three typical conductive walls, which were numbered 1, 2 and 3 and had

current values of −122 pA, −75 pA and −30 pA, respectively, can be observed. The subsequent V-PFM phase image in Figure 2b shows the formation of a head-to-head 71° charged wall at region 1, but head-to-tail 71° neutral walls were formed at regions 2 and 3 by variants of r1− and r2−, where the wall 2 is more conductive than the wall 3. The careful study of the lower left-corner domains in Figure 2a suggests a bunch of r1- and r2- domains to appear during CAFM scanning which then shrank into a single r2- domain during subsequent PFM imaging in Figure 2b. Therefore, all three r2- domains in Figure 2b that could coalesce together during poling collapsed during the very long measurement time (~1 h) of CAFM and V-PFM imaging. This is accompanied by the generation of intermediate bunched domains in Figure 2a. The bunched domains including the wall 2 are partially uncompensated so that they are more conductive than the isolated neutral wall 3. The conductivity enhancement due to the collapse of the switched bulk domain can be evidenced from the sudden enhancement of the "on" currents during backward sweeping of I-V curves (for example, the appearance of a small peak at -1.2 V in the left panel of Supplementary Figure S5a). [Rev1-8] These results unambiguously show that the charged wall is much more conductive than the neutral walls.

2.3 Angular dependence of wall current

The second approach will now be described. The AFM topographical image in **Figure 3**a (left panel) shows the rugate terrace structure of the film from the BFO (110)/STO (110) sample, which has a root-mean-square roughness value of 1.94 nm. The out-of-plane and in-plane V-PFM phase images in the right panel show that the entire BFO film is composed of the r4− monodomain. Because the film has this complete monodomain configuration, the angle (α) between the in-plane polarization $\boldsymbol{P}$ // [001] and the direction of the electric field $\boldsymbol{E}$ can be controlled by fabricating TE1 and TE2 to have different α values, as shown in Supplementary

Figure S6. Figure 3b (left panel) shows the *I*-*V* curves for devices with different α values and *w*/*l* = 200 nm/200 nm. Both the coercive voltages and the "on" currents of these devices increased nonlinearly with increasing α value from 0 to 90°, as illustrated by the plots in the right panel. The maximum "on" current at α= 90° was as high as ~300 nA for the nanodevices with their various *l* values (where *w* = 150 nm), as shown in Figure 3c (left panel), which was stable against the switching cycles (Supplementary Figure S7).[Rev1-7] At α= 45°, the wall current is on the order of 9.6 nA, comparable to 14 nA for the BFO (001)/STO (001) with TE1 and TE2 aligned along the <100> directions.[6] [Rev3-2] The voltage V_{c3} decreases with decreasing *l*, as shown in the inset. This high wall current eases high-speed reading of ferroelectric-resistive memory devices.

The α-dependence of the "on" current can be understood on the basis of the geometrical effect of the 180° domain wall relative to the original polarization direction of the BFO (110) film and the direction of the applied field. When the polarization of a local portion of the ferroelectric film is reversed by the applied field, the boundary between the two domains can be charged because of the uncompensated head-to-head and tail-to-tail configuration of the polarization, which induces a strong depolarization field. For simplicity, the 180° domain is assumed here, but identical arguments can be applied to the 71° and 109° domains, in which the stability is also influenced by the ferroelastic energy. As shown in Figure 3c (the first figure in the right panel in Figure 3c), when α = 0°, the ferroelectric bound charges of the locally reversed domain are readily compensated by the free carriers in TE1 and TE2. The remaining neutral 180° walls (indicated by the dotted red arrows in the α = 0° case) do not have any driving force to draw the free carriers, which makes the wall less electrically conductive. In contrast, when α = 90° (the second figure in the right panel in Figure 3c), the ferroelectric bound charge can hardly be compensated by the free carriers in the electrode, which leaves the depolarization field at a

maximum. The strong depolarization field, therefore, attracts the residual carriers in the film towards the charged 180° domain boundaries, which then makes the wall extremely conductive. The question thus arises as to how the reversed domain can be formed as shown in the figure, i.e., can the reverse domain be formed along the vertical direction while the electric field is applied along the horizontal direction? This could be possible when the local field distribution is taken into consideration, as shown in Supplementary Figure S8a-c and as described in the detailed discussions in Supplementary Section **F**. In short, the local field near the electrode edge contains a component in the vertical direction, even when the two TEs are located along the lateral direction. Based on the geometrical relationship between the actual field and α, the experimental V_{c3} is determined using $V_{c3} = \frac{V_c}{\sqrt{\cos^2\alpha + g^2\sin^2\alpha}}$, where V_c is the coercive voltage at $\alpha = 0°$ and g is an effective factor that is dependent on the variant position and the dielectric anisotropy along the [001] and $[1\bar{1}0]$ directions. From a solid-line fitting of the α-V_{c3} plot shown in Figure 3b (right panel), values of $V_c = 6.3$ V and $g = 0.33$ were derived.

In addition, the formal relationship between the "on" current and α can be derived by considering the depolarization field component in the direction perpendicular to the applied field. The detailed derivation and the related discussions are included in the Methods and Supplementary Section **E** in conjunction with Figure S6. Based on that formalism, the α-dependence of the "on" current when measured at a switching voltage of 20 V was simulated, with the results shown as the blue line in the right panel of Figure 3b. The precise matching between the experimental and model results demonstrates that the large wall current can be attributed to the presence of free carriers at the charge-uncompensated domain walls that connect the two electrodes.

2.4. Phase-field simulation of hierarchical domains

Many previous studies have indicated that domain switching in BFO begins from either 71° or 109° ferroelastic wall motion, which has a low energy barrier.[19, 25] The two barriers are initially quite close, which means that V_{c1} and V_{c2} can hardly be separated from the *I*-*V* curves during the first three to six sweeps (as shown in the left panel of Supplementary Figure S5a). After several tens of cycles, however, the two coercive voltages become discernible (as shown in the right panel of Supplementary Figure S5a). It can be assumed from the Landau-Lifshitz-Kittel law[26] that the minimum switched domain thickness at V_{ci} (where i = 1, 2 and 3) is proportional to the square root of *l*. Based on this assumption and the simulated horizontal field distribution (see Supplementary Figure S8a-c), the V_{ci}-l dependences can be fitted as shown by the solid lines in the inset of the left panel in Figure 3c and in Supplementary Figure S5d. The fitting parameters included the intrinsic coercive fields of 165 kV/cm, 252 kV/cm and 700 kV/cm that were assumed for the 71°, 109° and 180° domains, respectively. From the estimated V_c values for the different types of domains, the hierarchical domain evolution in the BFO (001)/GSO (110) structure, which had stripe domains between TE1 and TE2 after poling, can be examined quantitatively using a phase-field simulation (PFS). **Figure 4**a shows that the PFS can reproduce the general stripe domain pattern in the initially poled BFO (001)/GSO (110) structure contained within a nanodevice with w/l = 40 nm/44 nm (see the experimental data in Figure 1a), where the r2− and r3− domain variants are presented laterally. Upon application of a −5 V field, the electric field was found to reach a maximum at the centre of the gap, which then induced nucleation of the triangular r4− and r1− domains near TE2 through the 71° and 109° rotations of the original domains (see Figure 4b, in which the white coloured numbers indicate the rotation angles). As the applied voltage decreases to −7 V, as shown in Figure 4c, the rectangular r4− domain grew to form two mixed 71° and 109° walls that connected TE1 and TE2. Simultaneously, the r2+ variant

(i.e., the 180° reversal) that stems from the 71° and 109° rotations of the newly formed r4− and r1− variants appeared near TE1 as a result of local enhancement of the out-of-plane electric field strength. These results confirm that higher applied voltages lead to higher volume fractions of the 109° and 180° switched domains, in agreement with the V-PFM images of the switched domains shown in Figure 1b and c and Supplementary Figure S4b.

3. Discussion

Most of the domains in Figure 1b experienced the 71° rotation within the triangular region under application of a negative poling voltage between V_{c1} and V_{c2}. However, the domains near two small triangular corners experienced 109° rotations. This is due to the in-plane electric field inhomogeneity. The finite element simulation (Supplementary Figure S8a-c) shows the highest strength of electric fields near the two corners of TE2 along the directions that easily promote the reverse domain nucleation. The resulting reverse domain nucleation follows the paths of r3-→r2-→r1- and r2-→r3-→r4-, respectively, at the two corners. [Rev1-5]

The formation of hierarchical domains with dense conduction paths also contributed to the enhancement of the device reliability. When only one or two domain walls contributed to the electrical conduction with a high overall current level (> ~ 100 nA), the wall current density can reach the order of 5.6×10^4 A/cm^2 with the assumed wall width of 3.6 nm.[27] [Rev2-4] The nanodevice was easily damaged by the dielectric breakdown after such a high current flow for over 30 s. This was related with the severe local Joule heating (~6000 nJ) along the conduction path. However, when the number of involving paths was high by the hierarchical domain formation, this adverse effect was largely mitigated despite the overall current level was similar. This is due to the dividing of the high total current to the many conduction paths. Additionally, the accumulative

Joule heating effect would be significantly reduced to ~0.6 pJ if the domain switching time is shortened below 100 ns from pulsed characterization.Rev2-4

It has been reported that the electron mobility is ~0.2 $cm^2/(V \cdot s)$ in $SrTiO_3$ and 0.001 $cm^2/(V \cdot s)$ in $(Ba,Sr)TiO_3$ thin films.[1] The electron mobility of ~0.05 $cm^2/(V \cdot s)$ could be derived in this BFO film by fitting the "on" currents to the space-charge limited-current (SCLC) mechanism, which is in a reasonable agreement with the reported values (Experimental Section 5.4). Rev1-11

If the angular resolution of the in-plane rotating sample against the AFM cantilever was increased from 90° to 30° during the V-PFM performance, additional eight meta-stable polarization variants deviating from the <111> directions were detected,[6,28-30] where each variant has two or more neighboring domains.[31] Expectedly, these meta-stable polarization variants with large number of neighboring walls add more conductive paths to the "on" currents. Rev2-1

4. Conclusion

In summary, three different types of BFO thin films were prepared to study their hierarchical domain evolution behaviour upon application of a lateral voltage and to estimate the upper bound of the achievable "on" current through the charged domain walls. Intriguingly, the BFO (001)/GSO (110) sample provides a useful platform for quantitative examination of the domain configurations and the local conductivities of the walls as a function of applied bias voltage. Based on the estimated intrinsic coercive fields for the 71°, 109°, and 180° domain reversals, which are 165 kV/cm, 252 kV/cm, and 700 kV/cm, respectively, the hierarchical domain reversal via the 71° → 109° → 180° rotation was observed consistently. This represents a step forward in the understanding of the detailed domain evolution in BFO that has been enabled by the

combination of fabrication of optimum thin-film materials and use of state-of-the-art V-PFM and CAFM techniques. In addition, another BFO (110)/STO (110) sample with a monodomain configuration provided a practical and feasible method to examine the correlation between the charge compensation and the local electrical conductivity of the domain walls. It was confirmed that the head-to-head-type domain walls have high mobile carrier densities, as in doped semiconductors, which contributed to the extremely high wall currents of ~300 nA. The estimated carrier mobility at the charged domain walls was ~0.05 $cm^2/(V\cdot s)$. This is critical advancement in the field of resistance-based domain wall devices for use in ultra-high-density ferroelectric memories.

5. Experimental Section

5.1. Film growth

Epitaxial BFO films were deposited on (001) STO, (110) GSO, and (110) STO substrates by PLD using a KrF excimer laser with an operating wavelength of 248 nm. The laser, which was pulsed at 6 Hz, was focused with a power density of 2.8 J/cm^2 on a ceramic $Bi_{1.1}FeO_3$ target under oxygen pressure of 3 Pa. The typical film growth rate was ~1 nm/min. Films with thicknesses of between 35 nm and 120 nm were grown at an optimized substrate temperature of 602°C. XRD patterns were collected via θ-2θ scanning and reciprocal space mapping methods using a Bruker D8 Advance X-ray diffractometer with Cu-K_α radiation at 40 kV and 40 mA.

5.2. Nanodevice fabrication

After BFO film growth, 30-nm-thick Pt top electrode layers were grown on the BFO films by magnetron sputtering (PVD-75, Kurt J. Lesker) at 400°C. 200-nm-thick poly(methyl methacrylate) photoresist layers were subsequently spin coated on to the film surfaces. The TE1

and TE2 electrode patterns were then formed by electron beam lithography (EBL; 6300FS, JEOL) with an overlay accuracy of 20 nm. After patterning, 25-nm-thick Cr mask layers were deposited using a thermal evaporation system (NANO 36, Kurt J. Lesker) and a lift-off technique. Finally, the Pt regions that were not protected by these Cr mask layers were removed by ion milling using a reactive ion etching system (RIE-10NR, Samco). The shapes of the as-fabricated nanodevices were confirmed by scanning electron microscopy (SEM; Sigma HD, Zeiss) images.

5.3. V-PFM and CAFM characterization

The film morphology was measured under ambient conditions using an AFM in ScanAsyst-Air mode (Bruker Icon) and a silicon tip with a radius of 2 nm. V-PFM imaging of the diagonal domains in the BFO film was performed using a contact PtIr-coated silicon tip with a radius of 20 nm, a force constant of 2.8 N/m, and an alternating current (AC) signal at a frequency of 75 kHz and an amplitude of 10 V. Both the in-plane and out-of-plane domain images were captured after in-plane rotations of the sample at angles of 0° and 90°, respectively. Finally, a montage was used to convert all variants of the r1+/− to r4+/− domains across the film area with the evolution of the applied voltages. The exposed wall currents at the film surface were investigated using contact mode CAFM under a −5 V bias applied between TE1 and the AFM tip, where both the tip and TE2 were grounded. Each *I-V* curve was measured using an Agilent B1500A semiconductor analyser operating in voltage sweep mode with sweep times of 1-90 s.

5.4. Angular dependence of the "on" current

Carrier transport across the head-to-head walls can be modelled as a field-effect current along an n-type channel with a sub-threshold leakage current of[32]

$$I_D = I_0 e^{\frac{q(V_d - V_T)}{nk_B T}} \left(V_d < V_T\right), \quad (1)$$

where I_0 is the current at the threshold voltage V_T, n is the fraction of ($V_d - V_T$) that affects the barrier, k_B is the Boltzmann constant, q is the elementary charge, T is the temperature, and V_d is the depolarization voltage induced by a depolarization field applied perpendicular to the direction of current flow (Supplementary Figure S6). This type of relationship can be understood as a multiplication of the probability that the charged domain walls will capture the (free) carriers from the bulk region of the film {in the form of $\exp[q(V_d\text{-}V_T)/nk_BT]$} and the current transport along the wall when the read voltage V is applied between TE1 and TE2 (I_0). V_T is involved here because there is a kinetic energy barrier for the (trapped) carriers in the bulk BFO film to overcome to move towards the (created) charged domain wall, which is driven by V_d. V_d can be expressed as

$$V_d = \frac{2\delta P w}{\varepsilon_0 \varepsilon} \sin\alpha , \quad (2)$$

where δ ($0 \le \delta \le 1$) is an uncompensated factor of the polarization P, ε_0 is the vacuum permittivity, ε is the dielectric permittivity along the current path, and w is the distance (approximately equal to the electrode width) along the depolarization field. I_0 is dominated by the number of available carriers, particularly near the head-to-head wall,[7] in a manner following the space-charge limited-current (SCLC) formalism of

$$I_0 = \frac{9}{8} \varepsilon_0 \varepsilon \mu_e \theta w \Delta w \cdot \sin\alpha \cdot \frac{V^2}{l^3} , \quad (3)$$

where μ_e is the electron mobility, θ is the coefficient of charge trapping, w is the cross-sectional perimeter (approximately equal to the electrode width) of the charged wall, V is the applied

voltage between TE1 and TE2, and Δw is the wall thickness (approximately equal to nine unit cells).[27] For electron injection and trapping, θ is expressed as

$$\theta = g\frac{2P/\Delta w}{N_t}\exp(-\frac{\Delta E}{k_B T}), \tag{4}$$

where N_t is the trapped electron density, $2P/\Delta w$ is the doping density of the head-to-head wall, g is the degeneracy factor, and ΔE is the trap energy position below the donor level. In the trap-filled limit region that occurs because of the presence of oxygen vacancy-related trap levels, the power coefficient for V is larger than 2.[33] Because $\alpha = 0$, $I_0 = 0$. However, the neutral 180° walls generally demonstrate local side-way meandering behavior and contain kinks with head-to-head and tail-to-tail dipolar configurations that are locally charged,[34] which leads to a background wall current of I_B. Therefore, the total wall current is

$$I = I_D + I_B. \tag{5}$$

From Eqs. (1)–(5), the α-dependence of the "on" current was simulated as shown in Figure 3a–c. Under the assumptions that $V_d \approx V_T$, $\varepsilon = 93$, $P \approx 60$ μC/cm^2, and $\theta \approx 1$, μ_e was estimated to be approximately 0.05 cm^2/(V·s).

5.5. Phase-field simulation

The spatiotemporal evolution of the spontaneous polarization P_i can be obtained using the time-dependent Landau-Ginzburg-Devonshire equation of

$$\frac{\partial P_i(r,t)}{\partial t} = -L\frac{\partial F}{\partial P_i(r,t)} \qquad (i = 1,2,3), \tag{6}$$

where L is the kinetic coefficient, r is the position, t is the time, and F is the total free energy given by the following equation:

$$F = \int \left(f_{Landau} + f_{ela} + f_{ele} + f_{grad} \right) dV. \tag{7}$$

The bulk free-energy density f_{Landau} can be expressed using a sixth-order polynomial expansion [35,36], and the elastic energy f_{ela} can be obtained by solving the mechanical equilibrium equation of $\sigma_{ij.j} = 0$ under the boundary conditions that the thin film is stress-free at the top surface but is fully clamped at the bottom interface.[37] The electrostatic energy f_{ele} can be obtained by solving the Poisson equation of $\nabla^2\phi = \rho$, under the open-circuit boundary condition at the interface and the specified potential boundary condition at the top of the film[38], where φ is the potential and ρ is the charge density. The final term, f_{grad}, is the gradient energy. The simulations were performed in a system with dimensions of 256 nm×256 nm×100 nm and two rounded top electrodes (w/l = 40 nm/44 nm) with 1000 time steps (arbitrary units).

Supporting Information

Supporting Information is available from the Wiley Online Library or from the author.

Acknowledgements

The authors would like to thank Y. F. Chen for providing technical support in performing EBL and David MacDonald, MSc, from Liwen Bianji, Edanz Editing China (www.liwenbianji.cn/ac), for editing the English text of a draft of this manuscript.

Funding: This work was supported by the National Key Basic Research Program of China (grant number 2014CB921004), the National Natural Science Foundation of China (grant number 61674044), the Basic Research Project of Shanghai Science and Technology Innovation Action (grant number 17JC1400300), and the Program of Shanghai Subject Chief Scientist (grant number 17XD1400800). X.X.C and L.Q.C. acknowledge the support for the work at Penn State

from the U.S. Department of Energy, Office of Basic Energy Sciences, Division of Materials Sciences and Engineering under Award DE-FG02-07ER46417. J.F.S. acknowledges the financial support of the Strategic Priority Research Program of the Chinese Academy of Sciences (grant number XDB07030200). C.S.H. acknowledges the support of the Global Research Laboratory Program (grant number NRF-2012K1A1A2040157) of the National Research Foundation of the Republic of Korea.

Author contributions: A.Q.J. conceived the idea for the work and performed the electrical characterization, and, in conjunction with D.W.Z., L.Q.C, C.S.H, and J.F.S, directed the study and analysed the results. Z.L.B. grew the films, measured the XRD patterns, and performed the V-PFM measurements. X.X.C carried out the phase-field simulation. D.F.C performed the BFO nanodevice fabrication process. All authors discussed the results. A.Q.J. and C.S.H. wrote the manuscript.

Received: ((will be filled in by the editorial staff))
Revised: ((will be filled in by the editorial staff))
Published online: ((will be filled in by the editorial staff))

References

[1] J. F. Scott, *Ferroelectric Memories,* Springer, Berlin, GER **2000**.

[2] M. Gajek, M. Bibes, S. Fusil, K. Bouzehouane, J. Fontcuberta, A. E. Barthelemy, A. Fert, *Nat. Mater.* **2007**, *6*, 296.

[3] R. Soni, A. Petraru, P. Meuffels, O. Vavra, M. Ziegler, S. K. Kim, D. S. Jeong, N. A. Pertsev, H. Kohlstedt, *Nat. Commun*. **2014**, *5*, 5414.

[4] J. P. Velev, J. D. Burton, M. Y. Zhuravlev, E. Y. Tsymbal, *npj Computational Materials* **2016**, *2*, 16009.

[5] H. D. Lu, D. Lee, K. Klyukin, L. L. Tao, B. Wang, H. W. Lee, J. W. Lee, T. R. Paudel, L. Q. Chen, E. Y. Tsymbal, V. Alexandrov, C. B. Eom, A. Gruverman, *Nano lett.* **2018**, *18*, 491.

[6] J. Jiang, Z. L. Bai, Z. H. Chen, L. He, D. W. Zhang, Q. H. Zhang, J. A. Shi, M. H. Park, J. F. Scott, C. S. Hwang, A. Q. Jiang, *Nat. Mater*. **2018**, *17*, 49.

[7] R. G. P. McQuaid, M. P. Campbell, R. W. Whatmore, A. Kumar, J. M. Gregg, *Nat. Commun*. **2017**, *8*, 15105.

[8] A. Crassous, T. Sluka, A. K. Tagantsev, N. Setter, *Nat. Nanotech*. **2015**, *10*, 614.

[9] C. Godau, T. Kämpfe, A. Thiessen, L. M. Eng, *ACS Nano* **2017**, *11*, 4816.

[10] W. Wu, Y. Horibe, N. Lee, S.-W. Cheong, J. R. Guest, *Phys. Rev. Lett*. **2012**, *108*, 077203.

[11] D. Meier, J. Seidel, A. Cano, K. Delaney, Y. Kumagai, M. Mostovoy, N. A. Spaldin, R. Ramesh, M. Fiebig, *Nat. Mater*. **2012**, *11*, 284.

[12] T. Sluka, A. K. Tagantsev, P. Bednyakov, N. Setter, *Nat. Commun*. **2013**, *4*, 1808.

[13] P. Sharma, Q. Zhang, D. Sando, C. H. Lei, Y. Liu, J. Li, V. Nagarajan, *Sci. Adv.* **2017**, *3*, e1700512 .

[14] L. Li, J. Britson, J. R. Jokisaari, Y. Zhang, C. Adamo, A. Melville, D. G. Schlom, L. Q. Chen, X. Q. Pan, *Adv. Mater.* **2016**, *28*, 6574.

[15] S. Farokhipoor, B. Noheda, *Phys. Rev. Lett.* **2011**, *107*, 127601.

[16] J. Seidel, L. W. Martin, Q. He, Q. Zhan, Y. H. Chu, A. Rother, M. E. Hawkridge, P. Maksymovych, P. Yu, M. Gajek, N. Balke, S. V. Kalinin, S. Gemming, F. Wang, G. Catalan, J. F. Scott, N. A. Spaldin, J. Orenstein, R. Ramesh, *Nat. Mater.* **2009**, *8*, 229.

[17] J. B. Johnson, *Phys. Rev.* **1928**, *32*, 97.

[18] H. Nyquist, *Phys. Rev.* **1928**, *32*, 110.

[19] J. T. Heron, J. L. Bosse, Q. He, Y. Gao, M. Trassin, L. Ye, J. D. Clarkson, C. Wang, J. Liu, S. Salahuddin, D. C. Ralph, D. G.Schlom, J. Iniguez, B. D. Huey, R. Ramesh, *Nature* **2014**, *516*, 370.

[20] P. Bednyakov, T. Sluka, A. Tagantsev, D. Damjanovic, N. Setter., *Adv. Mater.* **2016**, *28*, 9498–9503.

[21] M. P. Campbell1, J. P. V. McConville, R. G. P. McQuaid, D. Prabhakaran, A. Kumar, J. M. Gregg, *Nat. Comm.*, **2016**, *7*, 13764.

[22] M. Park, K. No, S. Hong, *AIP Advances* **2013**, *3*, 214.

[23] M. Park, S. Hong, J. A. Klug, M. J. Bedzyk, O. Auciello, K. No, A. Petford-Long, *Appl. Phys. Lett.* **2010**, *97*, 112907.

[24] I. Stolichnov, M. Iwanowska, E. Colla, B. Ziegler, I. Gaponenko, P. Paruch, M. Huijben, G. Rijnders, N. Setter, *Appl. Phys. Lett*. **2014**, *104*, 132902.

[25] S. H. Baek, H. W. Jang, C. M. Folkman, Y. L. Li, B. Winchester, J. X. Zhang, Q. He, Y. H. Chu, C. T. Nelson, M. S. Rzchowski, X. Q. Pan, R. Ramesh, L. Q. Chen, C. B. Eom, *Nat. Mater*. **2010**, *9*, 309.

[26] V. Shelke, D. Mazumdar, S. Jesse, S. Kalinin, A. Baddorf, A. Gupta, *New Journal of Physics* **2012**, *14*, 053040.

[27] T. Rojac, A. Bencan, G. Drazic, N. Sakamoto, H. Ursic, B. Jancar, G. Tavcar, M. Makarovic, J. Walker, B. Malic, *Nat. Mater*. **2017**, *16*, 322.

[28] M. Park, S. Hong, _ J. A. Klug, M. J. Bedzyk, O. Auciello, K. No, A. Petford-Long, *Appl. Phys. Lett.* **2010**, *97*, 112907.

[29] M. Park, K. No, S. Hong, *AIP Adv*. **2013**, *3*, 042114.

[30] Y. Sharma, R. Agarwal, C. Phatak, B. Kim, S. Jeon, R. S. Katiyar, S. Hong, *Sci. Rep*. **2018**, *7*, 4857.

[31] B. Kim, F. P. Barrows, Y. Sharma, R. S. Katiyar, C. Phatak, A. K. Petford-Long, S. Jeon, S. Hong, *Sci. Rep*. **2018**, *8*, 203.

[32] B. L. Anderson, R. L. Anderson, *Fundamentals of Semiconductor Devices*. Tsinghua University, Beijing, CN 2006.

[33] J. Xing, H. Y. Hao, E. J. Guo, F. Yang, *J. Appl. Phys.* **2011**, *110*, 033103.

[34] J. Gonnissen, D. Batuk, G. F. Nataf, L. Jones, A. M. Abakumov, S. Van Aert, D. Schryvers, E. K. H. Salje, *Adv. Funct. Mater*. **2016**, *26*, 7599.

[35] R. K. Vasudevan, A. N. Morozovska, E. A. Eliseev, J. Britson, J-C. Yang, Y-H. Chu, P. Maksymovych, L. Q. Chen, V. Nagarajan, S. V. Kalinin, *Nano letters* **2012**, *12*, 5524.

[36] D. V. Karpinsky, E. A. Eliseev, F. Xue, M. V. Silibin, A. Franz, M. D. Glinchuk, I. O. Troyanchuk, S. A. Gavrilov, V. Gopalan, L. Q. Chen, A. N. Morozovska, *npj Computational Materials* **2017**, *3*, 20.

[37] Y. L. Li, S. Y. Hu, Z. K. Liu, L. Q. Chen, *Acta Materialia* **2002**, *50*, 395.

[38] Y. L. Li, S. Y. Hu, Z. K. Liu, L. Q. Chen, *Appl. Phys. Lett.* **2002**, *81*, 427.

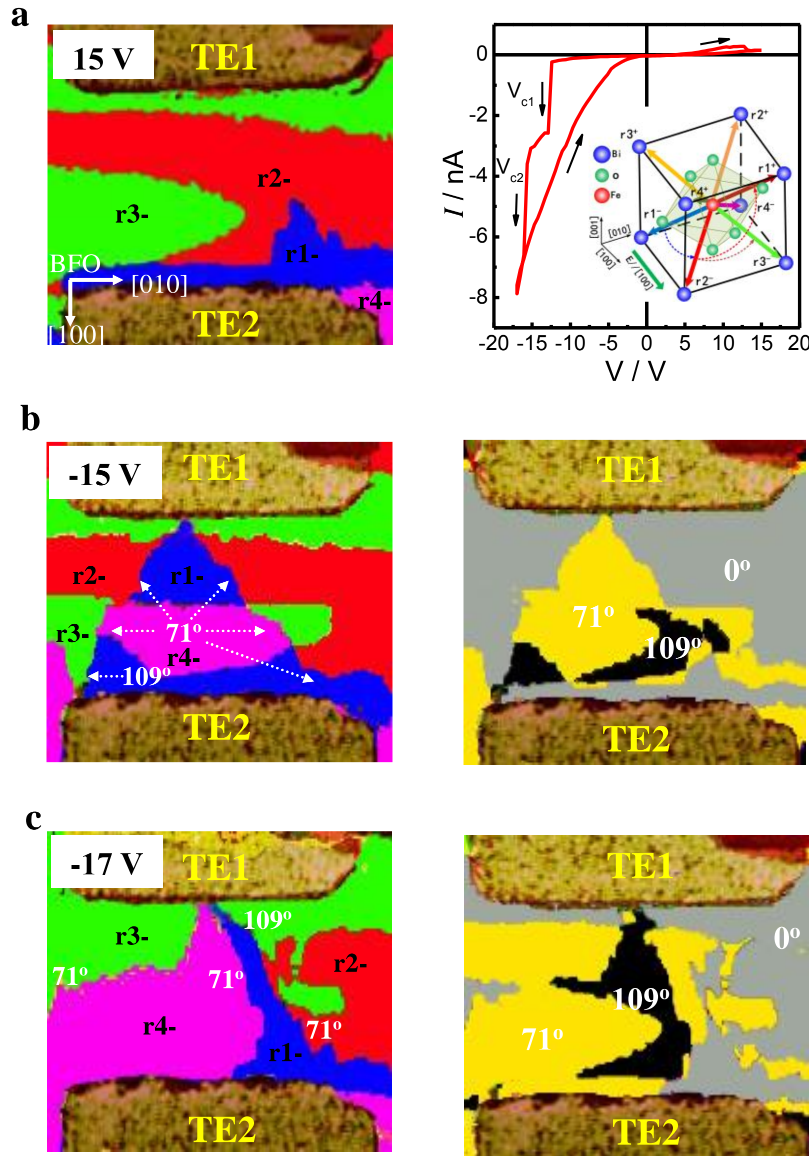

Figure 1. V-PFM phase images of polarizations of 120-nm-thick BFO (001)/GSO (110) nanodevices. (a) Initial stripe domains after poling at +15 V (left panel) with the domain configurations of r1−, r1+, r2−, r2+, r3−, r3+, r4− and r4+ within the nanogap (w/l= 1000 nm/500 nm) indicated by the coloured arrows in the inset of the right panel. The I-V curve (right panel) indicates the occurrence of two-step current jumps at V_{c1} and V_{c2} along the sweeping direction indicated by the black arrows. (b, c) V-PFM phase images of domain evolution under poling voltages of $V_{c2} < V < V_{c1}$ and $V < V_{c2}$, respectively, in formation of the 71° and 109° walls (left panels). The areal rotation angles of all variants are marked in the right panels.

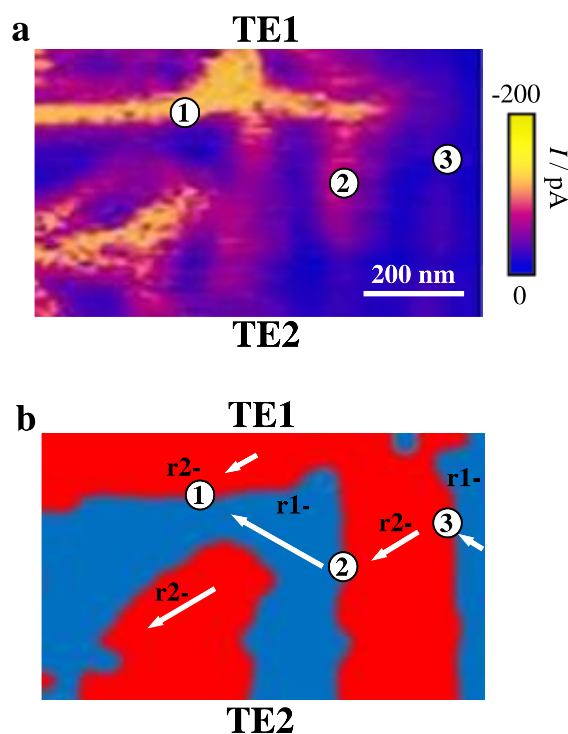

Figure 2. Current mapping of charged walls. (a) CAFM mapping image of wall currents at −5 V over the center region for the BFO (001)/GSO (110) nanodevice with $w \times l$ = 1000×1000 nm^2 after poling at −25 V. (b) V-PFM phase image of the newly formed 71° walls consisting of variants r1− and r2−.

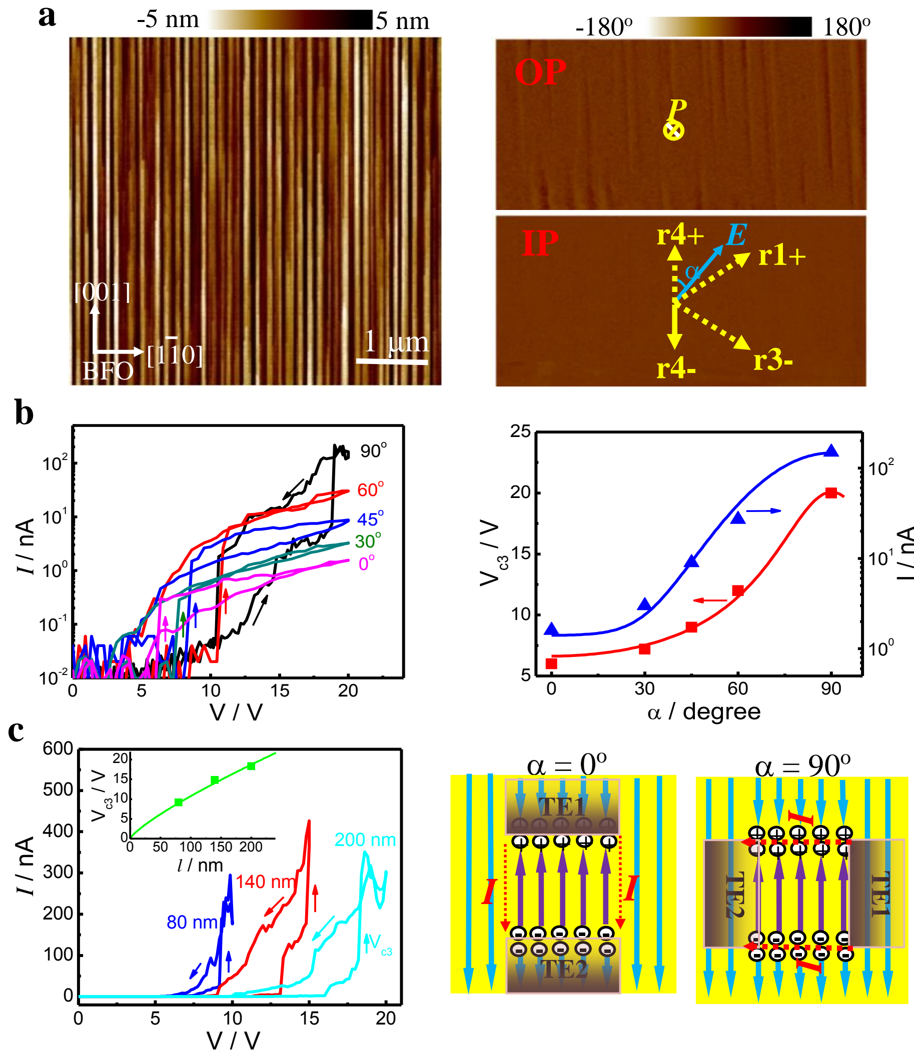

Figure 3. Angular dependence of wall current for BFO (110)/STO (110) nanodevices. (a) AFM topography (left panel) and out-of-plane (OP) and in-plane (IP) PFM phase images (right panel) of the film in a single domain pattern. The yellow-coloured arrows in the right panel indicate the successive rotations of the variant r4− into r3−, r1+, and r4+ under ***E***. (b) Angular dependences of the *I*-*V* curve (left panel), the coercive voltage, and the wall current at 20 V (right panel) for nanodevices with w/l = 200 nm/200 nm. (c) *I*-*V* curves at α=90° for nanodevices with various l but with a constant w of 150 nm (left panel), where the inset shows the l-V_{c3} dependence. The right panel shows the formation of the neutral and charged walls at angles of 0 and 90° that cause the wall currents to vary because of the 180° reversal of the central domain (purple arrows) against the unswitched peripheral domain (blue arrows). All solid lines are formed by fitting of the data.[rev2-9]

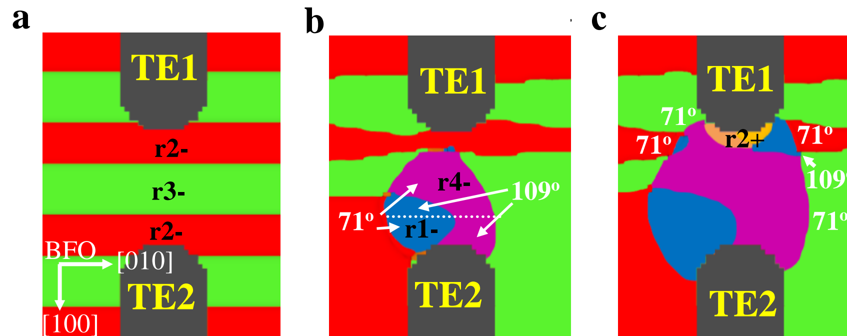

Figure 4. Phase-field simulations of multistep domain switching on GSO (110) substrates. (a) Initial stripe pattern of pristine domains r2− and r3−. (b) Triangular r1− and r4− domains within the nanogap with *w*/*l* = 35 nm/48 nm growing at −5 V through the 71° and 109° rotations of the pristine r2− and r3− domains near TE2. (c) The r4− domain penetrates throughout the entire gap length, forming mixed 71° and 109° walls to bridge TE1 and TE2 at −7 V. Simultaneously, the r2+ domain appears near TE1 at −7 V as a result of the rotations of the newly formed r1− and r4− domains, completing the 180° reversal of the pristine r2− domain.

Domain wall current in ferroelectric $BiFeO_3$ thin films can be magnified by two orders of magnitude through the careful selection of current flowing paths along the charged walls. The dense walls come into form through the hierarchical evolution of the 71°, 109° and 180° domains after multiple 71°rotations.

Keyword: hierarchical domains; domain wall; multiple rotations; wall current; ferroelectric domain-wall memory

Zi Long Bai, Xiao Xing Cheng, Dong Fang Chen, David Wei Zhang, Long-Qing Chen, James F. Scott, Cheol Seong Hwang*, An Quan Jiang*

Hierarchical domain structure and extremely large wall current in epitaxial $BiFeO_3$ thin films

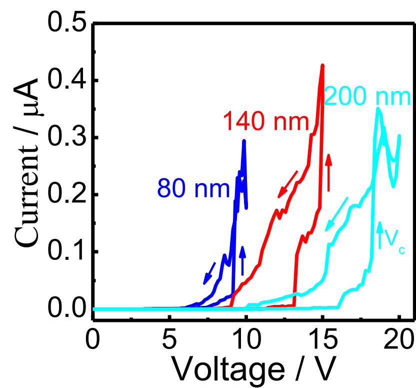

Supplementary Information

Hierarchical domain structure and extremely large wall current in epitaxial $BiFeO_3$ thin films

Zi Long Bai, Xiao Xing Cheng, Dong Fang Chen, David Wei Zhang, Long-Qing Chen, James F. Scott, Cheol Seong Hwang, An Quan Jiang**

Materials and Methods

A. Film growth.

B. Conductivity comparison between pristine walls and newly formed walls

C. V-PFM imaging of hierarchical domains.

D. 71°, 109° and 180° domain rotations inferred from *I-V* curves

E. Depolarization field and wall current

F. Domain switching at α=90°

G. Summary of rotation angles and walls

H. References

A. Film growth.

Epitaxial BFO thin films were deposited on (001) $SrTiO_3$ (STO), (110) $GdScO_3$ (GSO) and (110) STO substrates by pulsed laser deposition. The topographic atomic force microscopy (AFM) images in **Figure S1**a show the smooth film surfaces with terraces composed of atomic-scale steps. The X-ray diffraction (XRD) patterns shown in Figure S1b confirmed the preferred BFO (001) orientations on both the (001) STO and (110) GSO substrates and the (110) orientation on the (110) STO substrate.

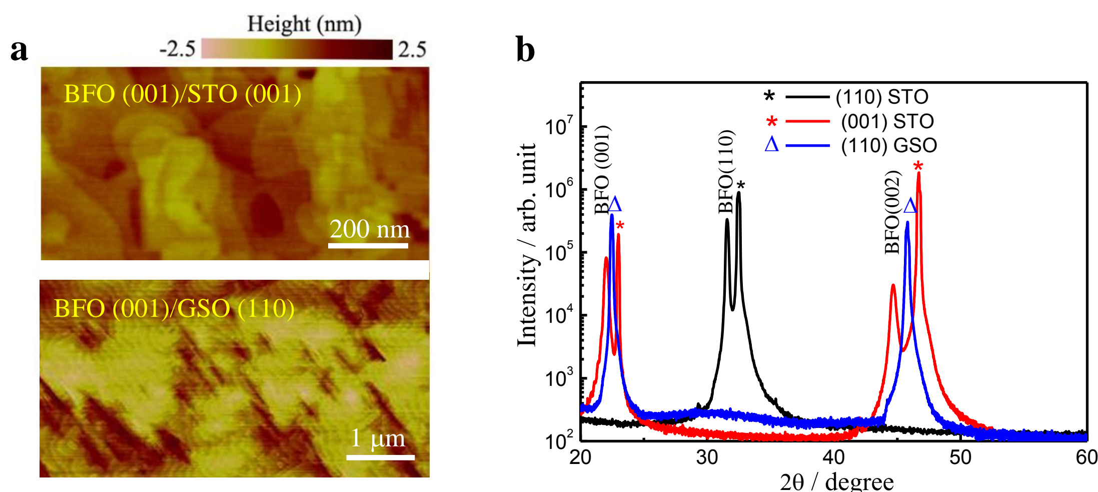

Figure S1. AFM and XRD characterization. (a) Topographic AFM images of the 35-nm-thick BFO (001)/STO (001) and 120-nm-thick BFO (001)/GSO (110) thin films. (b) XRD patterns of the epitaxial BFO thin films on the different substrates.

B. Conductivity comparison between pristine walls and newly formed walls

The pristine stripe domains in BFO (001)/GSO (110) consist of r1− to r4− variants, which can change into triangular and rectangular shapes via the local multiple 71° rotations of the domains under application of negative poling voltages in Figure 1b and c in main text. Normally, the pristine domains (r1− to r4−) can be rejuveated under application of a positive poling voltage

above +15 V. After switching at +/- 20 V for a dozen of cycles, there appear the newly formed r1- and r4- domains poled at +15 V, as shown in Figure 1a in main text, that are relatively stable against the switching cycles. However, the newly formed domains are unstable with relaxation time that could disappear after a few weeks, as shown in **Figure S2**.[Rev3-5]

The pristine stripe walls, that are less electrically conductive than the newly formed walls, were mostly compensated by charged mobile defects during film deposition at high temperature.[1] **Figure S3**a shows V-PFM images of the pristine stripe walls perpendicular to TE1 and TE2 after application of different poling voltages. There are six walls that initially connect TE1 and TE2 (left panel of Figure S3a) and these walls remain nearly unchanged at poling voltages between −5 V and −7 V (middle panel of Figure S3a). However, when the poling voltage becomes smaller than −12 V, several of these walls disappear (right panel of Figure S3a). Subsequent *I*-*V* curves shown in Figure S3b indicate that the current ($I_{\perp,\mathrm{on}}$) in the stripe walls that are perpendicular to TE1 and TE2 is much smaller than the "on" current in the newly formed walls ($I_{//,\mathrm{on}}$) but is slightly higher than the "off" current ($I_{//,\mathrm{off}}$) in the pristine stripe walls that are oriented parallel to TE1 and TE2 in Figure 2a–c in the main text.

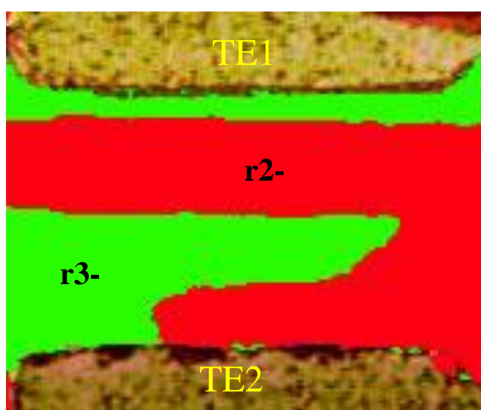

Figure S2. V-PFM phase images of polarizations of 120-nm-thick BFO (001) /GSO (110) nanodevices. Stripe domains in Figure 1a in main text restored into the pristine structure consisting of variants r2- and r3- only after retention time of 2 months.

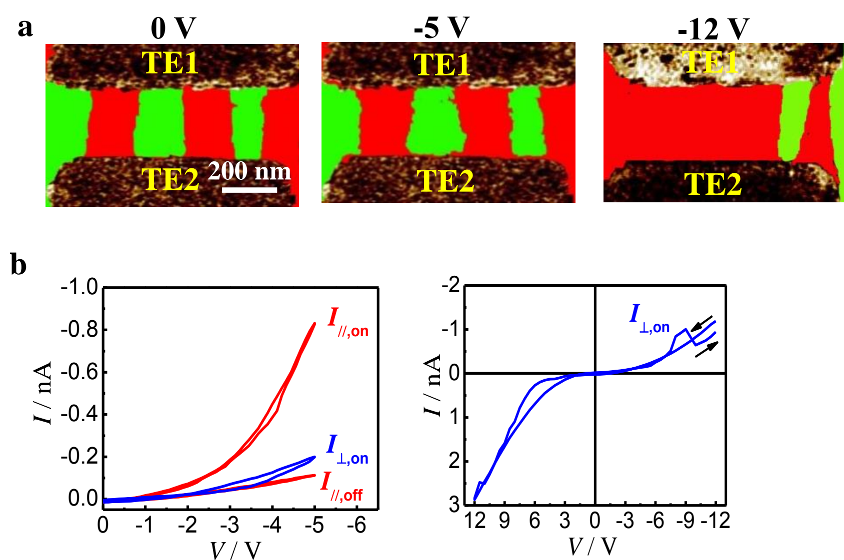

Figure S3. Wall currents of pristine stripe walls and newly formed walls in the BFO (001)/GSO (110) nanodevice. (a) V-PFM images of pristine stripe walls perpendicular to TE1 and TE2 after application of different poling voltages. (b) *I-V* curves for pristine stripe walls oriented perpendicular ($I_{\perp,on}$) and parallel ($I_{//,on}$ and $I_{//,off}$) to TE1 and TE2.

C. V-PFM imaging of hierarchical domains.

The in-plane switched 180° domains that formed at voltages higher than V_{c3} showed retention times that were too short to allow V-PFM images to be acquired for all the nanodevices fabricated on either the GSO or STO substrates at $l \leq 500$ nm. This is due to the influence of the strong depolarization field. However, when l is much larger than the film thickness (120 nm), the switched domains then become thick enough to reach the substrate at the bottom, which means that the depolarization field is greatly reduced.[2] In this way, the switched 180° domains could then be imaged by V-PFM. **Figure S4**a and b show V-PFM phase images of the switched domains within a nanodevice with w/l = 1000 nm/1000 nm. The initial r2− and r3− variants consist of 71° stripe domains after initial poling at + 20 V. A small area near TE2 contains the out-of-plane r3+ variant that persists permanently, even after bipolar poling of the device at ±20 V for a few cycles, as shown in Figure S4a (left panel). After switching at −20 V for 30 s, two hierarchical triangular r1− and r3+ domains appear in Figure S4b to form the four penetrating walls (mixed 71° and 109° walls) that connect TE1 and TE2 (left panel). The small gaps near TE1 occur because of domain shrinkage after removal of the switching voltage. This is due to the 71°, 109° and 180° rotations of the pristine r2− and r3− variants, as confirmed based on the areal distribution of the rotation angles in the right panel of Figure S4b. The right panel in Figure S4a shows the repeatable three-step jumps of the "on" current in the *I-V* curve. These results indicate that multiple 71° rotations of all variants will reach the final switched domain state.

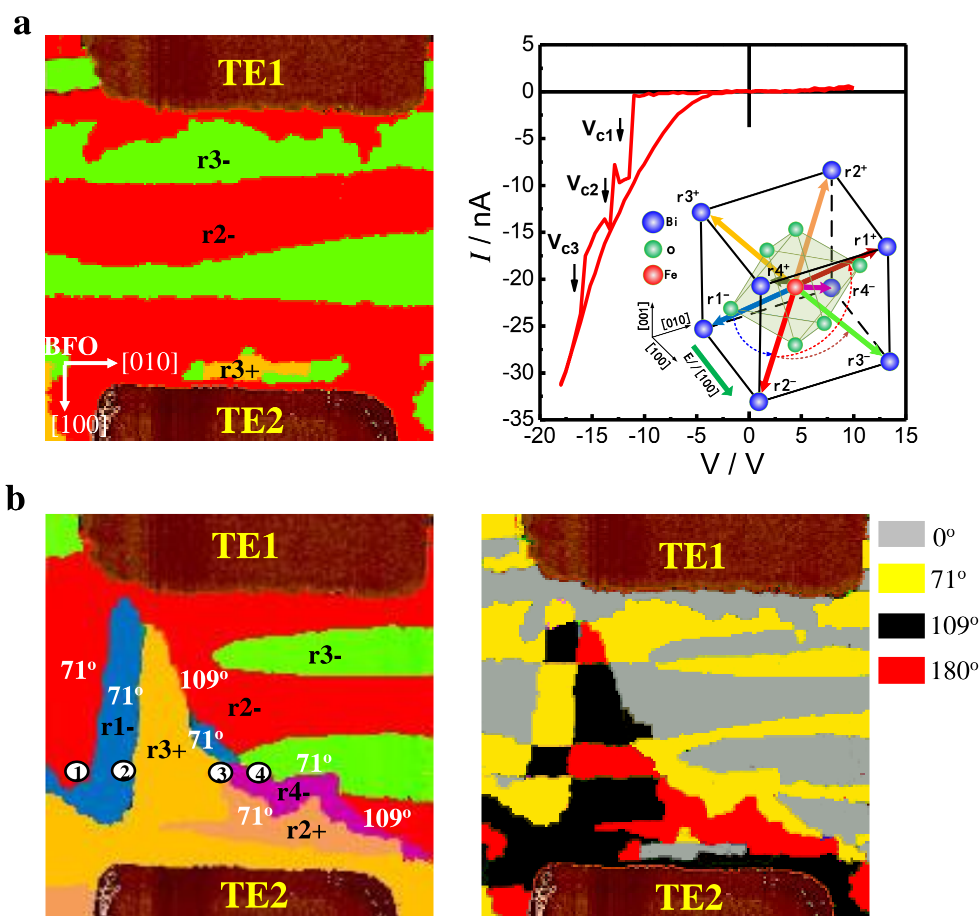

Figure S4. V-PFM phase images of polarization rotations for the BFO (001)/GSO (110) nanodevice. (a) Initial stripe domains with the polarizations in the left panel that correspond to the coloured arrows in the inset of the right panel after application of a poling voltage of +20 V. The right panel shows the repeatable three jumps of the "on" current in the *I*-*V* curve. (b) Appearance of the triangular r1− and r3+ domains that connect TE1 and TE2 using mixed 71° and 109° walls after application of the switching voltage of −20 V (left panel). The rotation angles of all variants are indicated in the right panel.

D. 71°, 109° and 180° domain rotations inferred from *I-V* curves

The growth of each of the penetrating domains in the region between TE1 and TE2 could increase the number of conductive walls and thus the "on" current in the *I-V* curves. **Figure S5**a–c show the *I-V* curves of the fabricated BFO (001)/STO (001) nanodevices produced by low-/high-voltage sweeping. The pristine domain patterns along the [100] direction (i.e., the preliminary written information) can be identified using in-plane V-PFM phase imaging (see the inset figures in Figure S5a–c). The V-PFM phase contrast shows the in-plane projection of the as-grown 71° domains, in which the black and white contrasts coincide with the spontaneous polarizations pointing from TE1 to TE2 and from TE2 to TE1, respectively. These opposite polarization directions induced the emergence of the "on" current at the opposite bias polarities, as will be discussed below.

Domain switching starts from either the 71°or 109° ferroelastic wall motion[3,4] with the two close coercive voltages of V_{c1} and V_{c2} that can be inferred from the two discrete jumps in the "on" current during the low-field sweeping of the *I-V* curves.[5] However, most of the nanodevices show only one current jump at −3.3 V during the first three *I-V* sweeps, as shown in Figure S5a (left panel). Meantine, one small peak occurring at -1.2 V in the backward sweeping of the *I-V* curve suggests the enhancement of the wall conductivity due to the collapse of the switched bulk domain (wall number enlargement). After a few tens of cycles, however, the two V_c values could clearly be discerned from the two abrupt increases in current at ~−2.7 V (V_{c1}) and ~−3.5 V (V_{c2}), which correspond to the coercive voltage (V_c) values of the hierarchical domains with lower V_c. At these voltages, in-plane transverse domain switching occurs to form the connecting domain walls within the gap region. However, under the application of a positive voltage, no reverse domains form because this bias direction is parallel to the initially projected polarization direction, and thus no current increase was observed. This also demonstrates that leakage current

conduction along the surface region of the film remained negligible as long as no domain walls form. In Figure S5b, a similar "on" current was observed at a much higher absolute voltage (V_{c3} ~−15 V) that corresponds to the 180° domain rotation, in addition to the occurrence of V_{c1} and V_{c2} at higher (absolutely lower) voltages. In addition, application of the positive bias did not induce the "on" current because the initial polarization direction of this device was identical to that of Figure S5a. In contrast, the device shown in Figure S5c shows similar switching and nonswitching current responses in opposite bias directions to those of the previous two cases because this device had the opposite initial polarization direction. The V_{ci} (i =1, 2 and 3) values that were estimated from multiple devices showed the nonlinear dependence of l, as illustrated in Figure S5d. Each "on" current can be fitted using the $I \propto V^n$ power law (where n = 2.5), as indicated by the black dashed lines in Figure S5a–c. The successive emergences of the three coercive voltages indicate the sequential formation of the 71°, 109° and 180° domains with increasing field strength. The "on" current value that was estimated at 12 V increased nonlinearly with decreasing l, following an $I \propto l^{-3}$ relationship, as indicated by the solid-line fitting of the data shown in Figure S5e. This is a typical characteristic of the space-charge-limited current (SCLC) mechanism.[6]

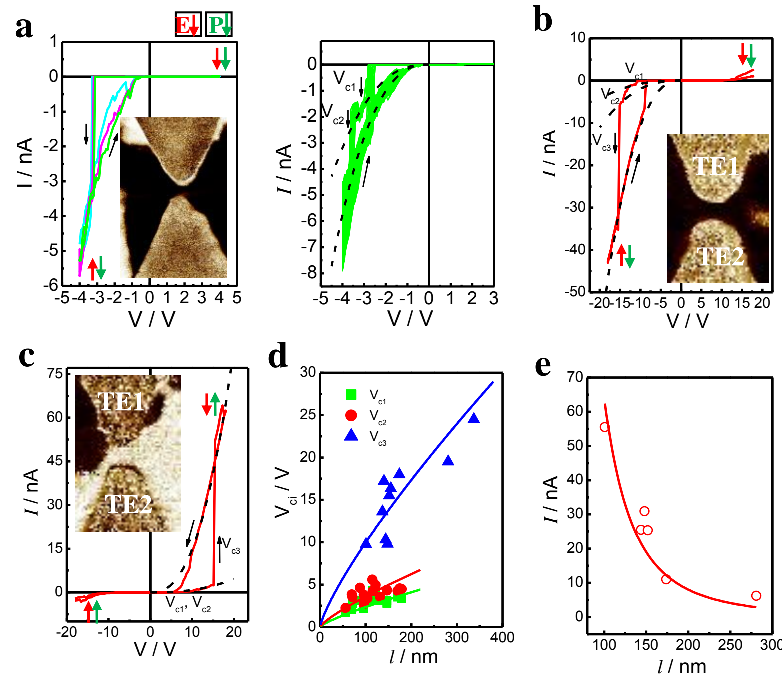

Figure S5. Multilevel "on" currents of 35-nm-thick BFO (001)/STO (001) nanodevices. (a-c) *I*-*V* curves of nanogaps with *w*/*l* configurations of 45 nm/71 nm, 88 nm/174 nm and 47 nm/152 nm, respectively. The first three sweeps in a show only one jump in the "on" current at −3.3 V (left panel) that split into two jumps after a few tens of cycles (right panel). Sweeping directions are indicated by black arrows, and the inset figures show in-plane V-PFM phase images of the positive (dark colour in a and b) and negative (white colour in c) projected polarizations within the gaps. The "on" and "off" currents occur when ***E*** is applied antiparallel and parallel to *P*, respectively. (d, e) Gap length dependences of the coercive voltages and the on-state current at 12 V with *w* = ~50 nm. All dashed and solid lines are the results of fitting.

E. Depolarization field and wall current

The central 180° domain reversal of the BFO (110)/STO (110) monodomain creates the charged walls, as shown in **Figure S**6, which then cause a strong depolarization field of $\boldsymbol{E}_{\mathbf{d}} = \boldsymbol{E}_{\mathbf{d}}^{\perp} + \boldsymbol{E}_{\mathbf{d}}^{//}$ (right panel), where $\boldsymbol{E}_{\mathbf{d}}^{\perp}$ and $\boldsymbol{E}_{\mathbf{d}}^{//}$ are the depolarization fields oriented perpendicular and parallel to the direction of flow of the wall current ***I***, respectively. Therefore, the head-to-head channel current (which is n-type) would be affected by two depolarization voltages given by

$$\begin{cases} V_d^{//} = \dfrac{2\delta P w}{\varepsilon_0 \varepsilon}\cos\alpha \\ V_d^{\perp} = \dfrac{2\delta P w}{\varepsilon_0 \varepsilon}\sin\alpha \end{cases}, \tag{1}$$

where δ is an uncompensated factor of the polarization P, ε_0 is the vacuum permittivity, ε is the dielectric permittivity, and w is the distance along the depolarization field. $V_d^{//}$ is the driving force for domain back-switching in the insulating regions when the applied voltage V between TE1 and TE2 is removed. This was not the case in the conductive channel regions, where $V_d^{//} = 0$ because of the full compensation of the domain boundary charges by sufficient numbers of free carriers. Therefore, the contribution of $\boldsymbol{E}_{\mathbf{d}}^{//}$ to the wall current is low. However, $\boldsymbol{E}_{\mathbf{d}}^{\perp}$ plays a significant role in accumulating sufficient free electrons to enhance the head-to-head wall conductivity. $\boldsymbol{E}_{\mathbf{d}}^{\perp}$ can also induce hole accumulation at the tail-to-tail p-type wall but bulk BFO is mostly n-type,[7] which means that hole accumulation is less likely.

The charged walls can be repetitively created. **Figure S7**a and b shows 10 sweeps of *I*-*V* curves for BFO (110)/STO (110) nanodevices at α=90° with l = 140 nm and 200 nm, respectively. All *I*-*V* curves can be generated repeatedly, but the nanodevices could be damaged if the accumulative *I*-*V* sweep time is over 100 s during continuous cycling.

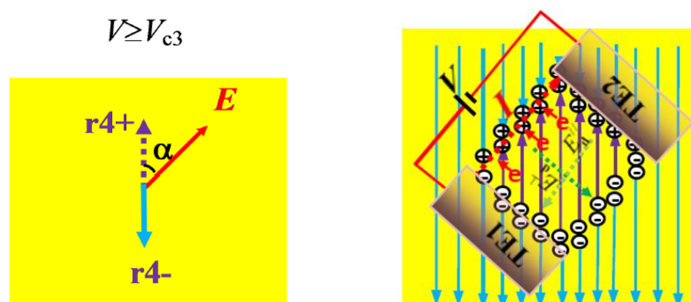

Figure S6. Field-effect wall current. 180° domain reversal induced by the electric field ***E*** produces two perpendicular depolarization fields, $\boldsymbol{E}_{\mathbf{d}}^{\perp}$ and $\boldsymbol{E}_{\mathbf{d}}^{//}$, where $\boldsymbol{E}_{\mathbf{d}}^{\perp}$ can accumulate free electrons to enhance the head-to-head wall conductivity.

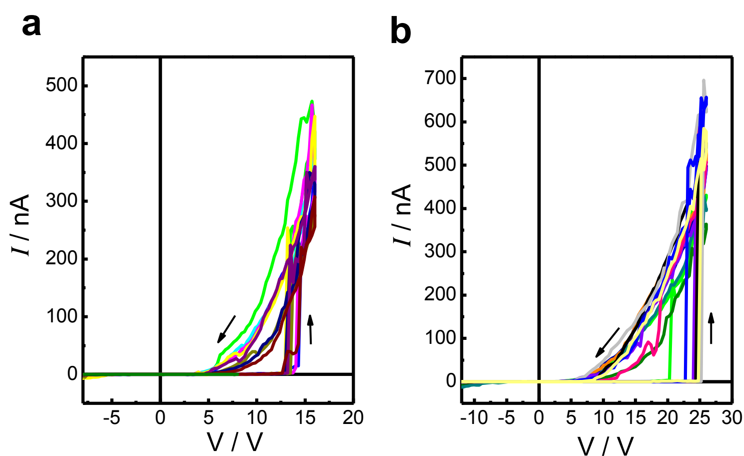

Figure S7. Repeatable *I-V* curves. 10 sweeps of *I-V* curves for BFO (110)/STO (110) nanodevices at α=90° with (a) l = 140 nm and (b) l = 200 nm but with a constant w of 200 nm.

F. Domain switching at α=90°

Finite element simulations determined the electric field (***E***) distribution required for reverse domain nucleation and growth between TE1 and TE2. Because of the wedge-shaped geometry of the TEs, ***E*** comprises radial and tangential electric fields (***E***// and ***E***⊥) within a local region. The presence of ***E***⊥, as shown in **Figure S8**a-c, means that reverse domain switching can be achieved even when α = 90°, as shown in Figure 3a–c in the main text. When the applied voltage is 5 V, the radial electric field strength is ~1000 kV/cm, which is strong enough to induce the initial 71° domain switching.[8] When the applied voltage increases up to 10 V, both the radial and tangential electric field strengths are strong enough to induce multiple 71° rotations of the local variant, which will eventually end up with 180° domain walls, even when α= 90°. The out-of-plane electric field strength is maximum near the two TEs, as shown in Figure S8c.

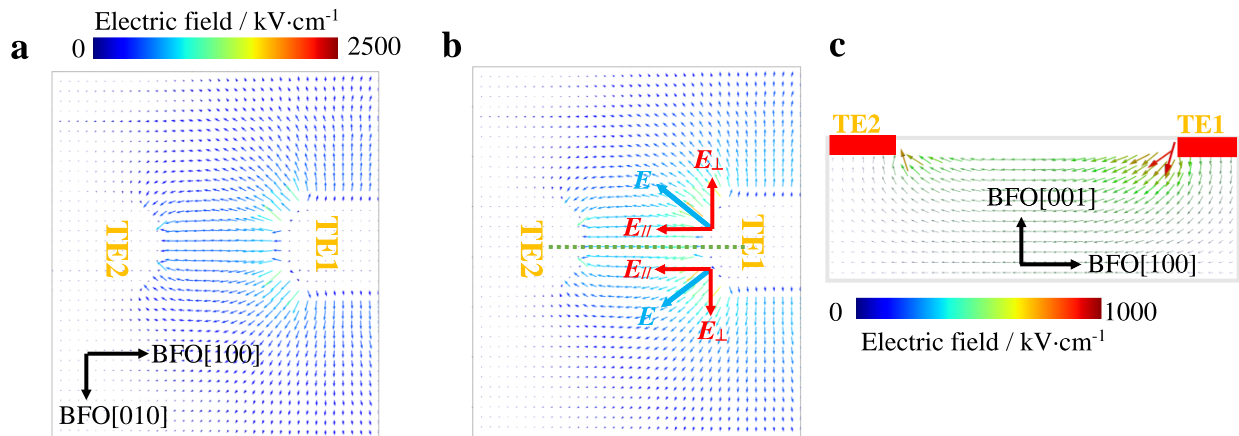

Figure S8. Finite element simulation of electric field distribution. The local electric field ***E*** within a nanogap with width/length of 35 nm/48 nm is composed of radial and tangential electric fields denoted by ***E***// and ***E***⊥, respectively, that both increase with enhanced applied voltages from (a) 5 V to (b) 10 V. (c) Cross-sectional electric field distribution along the dotted line in (b).

G. Summary of rotation angles and walls

Table I. Rotation angles and walls observed under various applied voltages

Figure	Variant	Rotation angle	Wall
Fig.2b	r2-→r1-	71°	71°
Fig.2b	r2-→r3-	71°	71°
Fig.2b	r3-→r4-	71°	71°
Fig.2b	r3-→r1-	109°	109°
Fig.2b	r2-→r3-	71°	71°
Fig.2b	r2-→r4-	109°	71°
Fig.2c	r2-→r3-	71°	71°
Fig.2c	r3-→r4-	71°	71°
Fig.2c	r2-→r1-	71°	71°
Fig.2c	r2-→r4-	109°	71°
Fig.2c	r3-→r1-	109°	71°
Fig.2c	r2-→r3-	71°	109°
Fig. S2b	r2-→r1-	71°	71°
Fig. S2b	r3-→r2-	71°	71°
Fig. S2b	r3-→r1-	109°	71°
Fig. S2b	r3-→r2-	71°	109°
Fig. S2b	r3-→r3+	180°	71°
Fig. S2b	r2-→r3+	109°	71°
Fig. S2b	r2-→r2+	180°	71°
Fig. S2b	r2-→r4-	109°	71°
Fig. S2b	r2-→r4-	109°	109°

H. References

[1] I. Stolichnov, M. Iwanowska, E. Colla, B. Ziegler, I. Gaponenko, P. Paruch, M. Huijben, G. Rijnders, N. Setter, *Appl. Phys. Lett*. **2014**, *104*, 132902.

[2] P. Sharma, Q. Zhang, D. Sando, C. H. Lei, Y. Liu, J. Li, V. Nagarajan, *Sci. Adv.* **2017**, *3*, e1700512 .

[3] J. T. Heron, J. L. Bosse, Q. He, Y. Gao, M. Trassin, L. Ye, J. D. Clarkson, C. Wang, J. Liu, S. Salahuddin, D. C. Ralph, D. G.Schlom, J. Iniguez, B. D. Huey, R. Ramesh, *Nature* **2014**, *516*, 370.

[4] S. H. Baek, H. W. Jang, C. M. Folkman, Y. L. Li, B. Winchester, J. X. Zhang, Q. He, Y. H. Chu, C. T. Nelson, M. S. Rzchowski, X. Q. Pan, R. Ramesh, L. Q. Chen, C. B. Eom, *Nat. Mater*. **2010**, *9*, 309.

[5] J. Jiang, Z. L. Bai, Z. H. Chen, L. He, D. W. Zhang, Q. H. Zhang, J. A. Shi, M. H. Park, J. F. Scott, C. S. Hwang, A. Q. Jiang, *Nat. Mater*. **2018**, *17*, 49.

[6] S. Farokhipoor, B. Noheda, *Phys. Rev. Lett.* **2011**, *107*, 127601.

[7] G. L. Yuan, J. L. Wang, *Appl. Phys. Lett*. **2009**, *95*, 252904.

[8] J. Wang, J. B. Neaton, H. Zheng, V. Nagarajan, S. B. Ogale, B. Liu, D. Viehland, V. Vaithyanathan, D. G. Schlom, U. V. Waghmare, N. A. Spaldin, K. M. Rabe, M. Wuttig, R. Ramesh, *Science* **2003**, *299*, 1719.